Nonlinear dynamics of locally pulse loaded square Föppl-von Kármán thin plates

N. Mehreganian[a], A. S. Fallah[b,c*], L.A. Louca[a]

[a] *Department of Civil & Environmental Engineering, Skempton Building, South Kensington Campus, Imperial College London, London SW7 2AZ, UK*

[b] *Department of Mechanical and Aerospace Engineering, Howell Building, Brunel University London, Uxbridge UB8 3PH, UK*

[c] *ICP Institute of Computational Physics, ZHAW Zurich University of Applied Sciences, Technikumstrasse 9, CH-8401 Winterthur, Switzerland*

Abstract

Modern armour graded thin steel plates benefit from significant elastic strength with high elastic energy storage capacity, which contributes to dissipation of total impulse from extensive blast loads within the bounds of the elastic region. Higher elastic energy storage capability mitigates the probability of catastrophic damage and ensuing large deformations compared to the conventional graded metallic panels. While blast assessment of such structures is important to design and application of protective systems, limited studies are available on their response to localised blasts.

The present paper aims at deducing, from the minimization of Föppl-von Kármán (FVK) energy functional, the dynamic response of localised blast loaded thin elastic square plates undergoing large deformations. The presumed blast load function is a multiplicative decomposition of a prescribed continuous piecewise smooth spatial function and an arbitrary temporal function which may assume various shapes (e.g. rectangular, linear, sinusoidal, exponential).

A kinematically admissible displacement field and the associated stress tensor were considered as a truncated cosine series with multiple Degrees-of-Freedom (DoF's). From the prescribed displacement field, having simply supported boundary conditions, useful expressions for stress tensor components were delineated corresponding to a unique mode and a series of differential equations were derived. The explicit solutions were sought using the Poincaré-Lindstedt perturbation method. The closed form solutions of each mode were corroborated with the numerical FE models and showed convergence when the first few modes were considered. The influence of higher modes, however, on the peak deformation was negligible and the solution with 3 DOF's conveniently estimated the blast response to a satisfactory precision.

---

[*] To whom correspondence should be addressed:
Email: arash.soleiman-fallah@brunel.ac.uk
Tel.: +44 (0)1895 266408

Keywords: Localised blast, Föppl Von-Kármán functional, membrane, Poincaré-Lindstedt method, armour steel, Multiple Degree-of-Freedom Model (MDoF)

Notations

The following symbols are used in this paper:

Latin upper and lower case		R_e	Loading constant (central) zone radius [L]
		Greek lower case	
A	Elemental area; [L^2]	α	Localised blast Load parameter; [1]
L	Plate half-length;[L]	ϵ	Perturbation parameter; [1]
D	Flexural rigidity; [ML^2T^{-2}]	$\phi_{mn}(x,y,t)$	Airy Stress function; [MLT^{-2}]
E	Young's modulus [$ML^{-1}T^{-2}$]	$\phi^*(x,y)$	Spatial part of Airy Stress function; [1]
H	Plate thickness; [L]	$\bar{\phi}(t)$	Normalised temporal part of Airy Stress function [1]
$W_{mn}(t)$	Temporal part of the displacement field; [L]	κ_x,κ_y	Curvature in x, y direction; [L^{-1}]
$a = e^{bR_e}$	Load shape constant; [1]		
b	Load shape decay exponent; [L^{-1}]	κ_{xy}	Warping curvature; [L^{-1}]
p_0	Maximum overpressure; [$ML^{-1}T^{-2}$]	μ	Areal density ($= \rho H$); [ML^{-2}]
$p_1(x,y)$, $p_1(r)$	Spatial part of pressure pulse load; [$ML^{-1}T^{-2}$]	ρ	Material density; [ML^{-3}]
$p_2(t)$	Temporal part of pressure pulse load; [1]	θ	Polar coordinate rotational angle [1]
$w^*_{mn}(x,y)$	Spatial part of the displacement field [L]	ν	Poisson's ratio; [1]
$\bar{w}_{mn}{}^{(i)}$	Normalised maximum mid-point displacement of i^{th} iteration [1]	ω_{mn}	Vibration frequency; [T^{-1}]
t_d	Duration of the load; [T]	τ_{mn}	Normalised vibration time; [1]
		$\bar{\omega}$	Pseudo vibration frequency; [T^{-1}]

1 Introduction

Mitigating the detrimental effects of extensive pulse pressure loads, such as blasts from near field explosives, is crucial due to the catastrophic localised damage to critical equipment and structural elements, as well as potential accompanied loss of life they cause. In the case of a localised blast, structural response is particularly sensitive to the stand-off distance, as the magnitude of blast-induced pressure decays exponentially with the distance between the target and the charge. Hence, localised blast loads impart a focused impulse from the point of projection to the localised regions of the target, leading to large deformations [1].

When the deformation of a structural element, such as a thin plate, is of a higher order of magnitude than its thickness, the element undergoes finite displacements (geometry changes) whereby of membrane (catenary) forces are evolved. The membrane forces so emerged will resist out-of-plane deformation and decrease maximum displacement at the cost of high in-plane tensile stresses [2].

Most protective structural systems, such as blast walls, shutters, doors, as well as armored vehicles components, are designed in the form of plated elements. These elements can be fabricated from ductile isotropic materials such as conventional steel or modern armour graded steel with high load bearing capacity beyond the initial yield point, leading to an elastic-plastic response. The former is characterized by a relatively low yield stress and a long plastic plateau while the latter possesses high yield strength and low ductility, whereby the elastic strain energy becomes significant.

In fact, for structural systems made of rate-insensitive materials (thus dynamic responses independent of strain rates) and no hardening, the constitutive tensor may be treated as that of elastic-perfectly plastic or rigid-perfectly plastic isotropic metals. As argued by Li et al [3] and Fallah et al [4], when the dimensionless structural response $\alpha = R_0/Ky_c$ (where R_0, K, y_c denote the resistance, stiffness, and critical deformation, respectively) is less than unity and the maximum pulse load P_m does not exceeds the structural resistance, the rigid-perfectly plastic simplification may not be applicable. In such circumstance, the quotient of the energy stored elastically in the system to the kinetic energy of the plate is noticeable [5]–[7].

Thus, while the elastic response of protective metallic structures against high amplitude dynamic loads is often ignored for simplicity, there are certain cases where such response should be retained in the analysis. Similarly, elastic analysis provides a useful insight into predicting the complex response of quasi-brittle, thin structural plate elements, such as glass panes, composites and thin armour steel. The latter is a suitable candidate material for blast protection as it bears high elastic energy capacity preceding its small plastic deformation[8], [9].

Yuan and Tan examined the response of elastic-perfectly plastic beams to uniform pulse pressure loads by extending the minimum Δ_0 technique from Symonds [10]. Three distinct phases of motion were assumed whereby the motion was classified into phase 1- elastic vibration, phase 2- perfectly plastic deformation and phase 3- residual elastic vibration. The influence of membrane stretching was only retained at phase 3 when the motion was characterised by travelling plastic hinges. Thus, the elastic and plastic responses were distinctly separated in each phase of motion, whilst the membrane stretching effects in the elastic regime was ignored.

The present study deals with applying the well-established Föppl Von-Kármán model to address the influence of finite displacement, or geometry changes in the overall response of the structure, in light of the developed membrane resistance in conjunction with the bending resistance of the structure.

In fact, the FVK model is particularly pragmatic to capture the pronounced variation of shell transverse deformation field with its membranal strains using the minimal geometric nonlinearity [11]. The scientific literature devoted to applications of this model spans from buckling and post-buckling of plates in aerospace engineering [12], [13] to blast response of laminate glass [14]–[16], from instabilities of composites under thermal loads [17] to wrinkling of soft biological tissues[18]. Recently, in the fields of aerospace, structural and mechanical engineering, the complex response of plates to blast loads of distinct types has been highlighted the limitations of classical theories and the need for consideration of geometric nonlinearities using the FVK model. This is particularly essential for structures where the contribution of the energy stored elastically through the plate to the total kinetic energy cannot be ignored. An example of this is the counter-intuitive behaviour of armour steel compared to conventional steel graded panels which ruptured at the same impulse despite the lower ductility and midpoint transverse deflection. [9].

Teng et al [19] examined the transient deflection of the simply supported and clamped square plates under a uniform blast load with exponentially decaying time function. The FVK expressions were reduced to Duffing equations using the variational techniques. The authors employed the Poincaré-Lindstedt perturbation method to analyse the plate response. While the transient deformation at the first approximation was concurrent with that of numerical models, prediction of the response was limited to the loading phase only. Feldgun et al. [20] developed an SDOF model for rectangular plates with various boundary conditions subjected to a uniformly distributed exponential pulse load. Static and dynamic analyses were developed and compared with the numerical models as well as the available experimental tests. However, the plot of deformation time history determined from the numerical solution of Duffing equation, using the Runge-Kutta method, revealed the increase in peak deformations over time. Any theoretical or numerical treatment of the problem of this kind should be couched in caveats, as the presence of secular terms (such as $tsin(t)$) would lead to unbounded growth of deformations and would not reflect the actual response of the structure. A similar phenomenon was observed in [21] which used Ultraspherical Polynomial Approximation technique on circular and square plates with various boundaries.

For high-dimensional nonlinear dynamic systems, due to the existence of modal interactions, different forms of vibrations may arise as a consequence of relationship between several types of internal resonant cases. A special internal resonant relationship between two linear natural frequencies may lead to large amplitude nonlinear response [22]. Wang et al [23] studied the transient response of doubly curved graphene nanoplatelet reinforced composite (GPLRC) shells upon the thermal effects of the blast loads. Based on Reddy's higher order shear deformation theory [24] and von Kármán's strain displacement expressions, a growth in the vibration amplitude with the increase in pulse duration, while diminishing the response frequency, is observed. Similarly, the temperature difference between the top and bottom surfaces of the GPLRC induced permanent transverse deformation on the shell. Liu et al [22] and Zhang et al [25], in parallel studies, investigated the visco-elastic response of composite laminated circular cylindrical shells with pre-stretched membranes due to periodic thermal effects. Based on the third order shear-deformation theory, Galerkin's method and Poincaré's perturbation theory, the periodic and chaotic motions were observed depending on the temperature variation in the interval of 15-70^{o}K/^{o}C. Zhang et al [26] used the same theory to study the chaotic motion of orthotropic plates due to transverse and in-plane excitations. The existence of chaotic response was confirmed for certain transverse excitations.

Linz et al [14] presented experimental and numerical studies on the performance of laminated glass subjected to uniform blast loads. The Material properties (average stiffness, Poisson's ratio and average areal density) of the full composite action were estimated as an average of the properties of each lamina (consisting of glass and Polyvinyl Butyral (PVB)). The analytical model employed FVK expressions to capture the PVB membranal forces and maximum deformations. The authors assumed a truncated series of cosine functions to represent the displacement field of the structure. The assumption of using a single term for the deformation and Airy stress function series pragmatically estimated the response for the lower intensity blasts to characterize the pre-crack behaviour of the composites. However, the Digital Imaging Correlation from experiments showed that such a deflection shape would not be suitable for more intense loading. The curvature field from DIC was non-uniform with curvature concentration on the plate edges. However, the analytical model was sparse, i.e. the post loading behaviour of the plate was not investigated analytically. Clearly, the transient pulse loading induced dynamic response is a two-step process which consists of an undamped forced- and free-vibration, the latter occurring beyond fluid-structure separation. The visco-elasticity (damping effects) would not contribute to the elastic energy dissipation due to the short duration response although it kills it off in the subsequent cycles.

Over the past decades, the literature concerned with the performance of structures subject to blast loads have mostly dealt with pulse pressures of uniform distribution across the target, which is pertinent to the blasts charges with stand-offs more than the half-span of the structural element [27]. However, the physics of localised blast is complex as the response is contingent upon, and sensitive to, the load parameters characterising the spatial and temporal distribution of the dynamic pressure.

Thus, the objective of this work is to examine the explicit solutions of geometrically nonlinear elastic, isotropic homogeneous square plate to localised blast load. The plates investigated here are assumed thin, where the terms of transverse shear from the Mindlin-Reisner plate theory can be neglected, but as the blast loads incur damage and deformation in high order of the plate thickness, the influence of finite displacements, or geometry changes, due to the presence of membranal forces must be retained in the analysis conducted. This is achieved by implementing the well-known Föppl-Von Kármán (FVK) nonlinear theory.

The current paper is organized in 6 sections and entails a description of the localised blast in section 1, followed by the derivation of the governing equations of membrane elasticity in section 2. In Section 3, the theoretical solutions at two distinct phases of motion are investigated, while the pulse shape effects were examined in section 4. The theoretical solutions were validated against the Finite Element numerical models in Section 5. Finally, the concluding remarks of the study are presented in Section 6.

1.1 Localised blast load

Typical blasts associated with chemical exothermic reactions rapidly release a significant amount of energy which generates an overpressure, i.e. pressure beyond the atmospheric pressure, at a given stand-off distance followed by monotonic decay back to the ambient pressure. A wide range of experimental data by Kingery and Balmash provided reference to describe the air blast parameters through empirical equations. The empirical relations represented the blast load parameters of given TNT equivalent charge using the Hopkinson-Cranz scaling parameter. However, these data were limited to the range of parameters investigated, while the blast wave interaction with the target was restricted to infinite reflecting surfaces (no reflection) [28], [29].

The blast load function in this study is truncated into a single term of multiplicative decomposition of its temporal (pulse shape) and spatial (load shape) functions. The load shape parameters depend on the proximity of the blast source whilst the pulse shape is influenced by the characteristics of the blast source, namely as either deflagration, such as gas explosion giving rise to a pulse shape with finite rise time depending on the stoichiometric composition of the ambience, or detonation (high explosives explosion with virtually zero rise time and exponentially decaying pulse shape). The pulse shape has no intrinsic effect on the response for impulsive blasts, i.e. when loading duration is small ($t_d \rightarrow 0$). In such circumstances, the pressure would be idealised with Dirac delta function. The assumed spatial variation of the load, as shown by Eq. (1) and in Fig. 1, maintains a uniform pressure within the central disk of radius r_e before decaying exponentially along radial coordinate (r) [2], [8], [30]–[32]. We also examine the influence of pulse shape and show the significant difference between the response due to various pulse shapes for a purely elastic body.

In fact, the literature on the pulse shape profiles and pressure time histories is rich. Schleyer and Hsu [33] presented an experimental study of dynamic pressure load type of confined gas explosions. The plate resisted the loading primarily by elastic membrane and no noticeable yield line/plastic hinges were formed. Aune et al. [29], [34] presented studies on the response of aluminium alloys based on experimentally obtained pressure time-history data using the Digital Image Correlation (DIC) technique. Yuan and Tan discussed Youngdahl's technique [35], [36] to eliminate the pulse shape influence to be valid only for monotonically decaying pulse [37].

The plated structure studied here comprises an initially flat, monolithic, ductile metallic square plate with side length $2L$, thickness of H and areal density of $\mu = \rho H$. The plate is secured along its periphery with simply supported boundary conditions and subject to a localised pulse pressure load. Thus, the load is axisymmetric and reduces the domain of study to only one quarter of the plate (considering the square plate has 4 axes of symmetry).

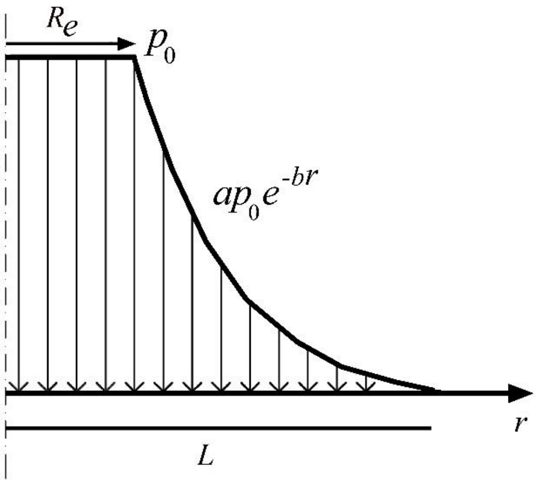

Fig. 1- Spatial distribution of load

$$p_1(r) = \begin{cases} p_0 & 0 \le r \le R_e \\ p_0 a e^{-br} & R_e \le r \le R \end{cases} \tag{1}$$

$$p_2(t) = \begin{cases} 1 & for\ 0 \le t \le t_d \\ 0 & for\ t \ge t_d \end{cases} \tag{2}$$

For simplicity, the negative phase of the pulse load is ignored as its influence is deemed negligible in the event of localised blasts. Using the Ritz-Galerkin's method, load functional is minimised in Eq. (3). The load is rotationally symmetric, thus independent of the polar coordinate θ. Hence, while the integral may be easily evaluated for two asymptotic cases, i.e. considering (i) the square plate of half-length L equal to that of a circular one with radius R, and (ii) the radius being $R = \sqrt{2}L$. The actual value is bounded between the two. In fact, the difference between the evaluated integrals for the two cases in most scenarios is infinitesimal and may be ignored. For accurate evaluation of the actual integral by implementing the transformation of coordinates, such a functional may be furnished into a single dimensionless parameter α in Eq. (4), influenced by the central constant load radius R_e as well as the load decay exponent b, expressed.

$$\begin{aligned} \int\int_{(A)} p(x,y,t)\delta w dA &= \int\int_A p_0 \cos\left(\frac{\pi x}{2L}\right)\cos\left(\frac{\pi y}{2L}\right)dxdy + \int\int_A p_1(x,y)\cos\left(\frac{\pi x}{2L}\right)\cos\left(\frac{\pi y}{2L}\right)dxdy \\ &= \int_0^{\frac{\pi}{2}}\int_0^{R_e} p_0 \cos\left(\frac{\pi r cos(\theta)}{2L}\right)\cos\left(\frac{\pi r sin(\theta)}{2L}\right) r dr d\theta \\ &\quad + \int_0^{\frac{\pi}{2}}\int_{R_e}^{L} p_0 e^{-(br - bR_e)}\cos\left(\frac{\pi r cos(\theta)}{2L}\right)\cos\left(\frac{\pi r sin(\theta)}{2L}\right) r dr d\theta = \alpha p_0 L^2 \end{aligned} \tag{3}$$

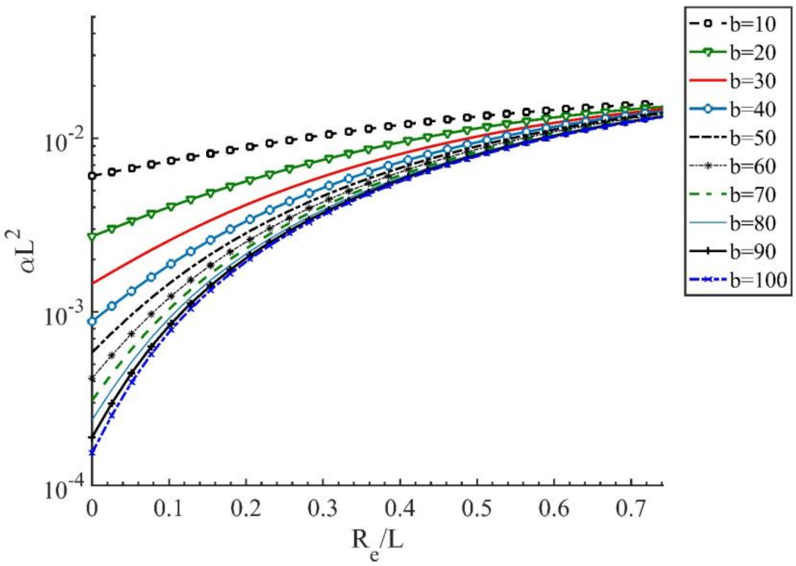

Fig. 2- Influence of the load parameters on the value of α with $L = 0.2$

It can be seen in Fig. 2 that various values of α converge to a unique value pertinent to the case of uniformly distributed load as $R_e \to L$, independent of the decay type.

$$\alpha = \frac{1}{b^2L^2(2L^2b^2+\pi^2)^2}\left[32\left(\left(\frac{1}{16}\pi^4 bR_e + \frac{1}{4}L^2b^2(bR_e+3)\pi^2 + L^4b^4\right)cos\left(\frac{\pi R_e}{2L}\right) + \frac{1}{2}\pi bL\left(\left(\frac{1}{4}bR_e - \frac{1}{2}\right)\pi^2 + L^2b^3r_e\right)sin\left(\frac{\pi R_e}{2L}\right) + \frac{1}{8}\pi^3\left(b^2L^2 + 2Lb + \frac{1}{4}\pi^2\right)e^{-b(L-R_e)} - \left(b^2L^2+\frac{1}{4}\pi^2\right)^2\right)\right] \quad \textbf{(4)}$$

2 Governing Equations

The general expression for the Cartesian components of the strain tensor is given as:

$$\varepsilon_{ij} = \frac{1}{2}(u_{i,j} + u_{j,i} + u_{k,i}u_{k,j}) \quad \textbf{(5)}$$

where $\boldsymbol{u}(x_i, t)$ is the displacement field and the comma in subscripts denotes differentiation with respect to the coordinate that follows, i.e. $u_{i,j} = \partial u_i/\partial x_j$. For convenience, the components of tensors, in the reference space in indicial notation $\mathcal{C}(i,j,k)$ may be replaced by those in von Kármán notation $\mathcal{C}(x,y,z)$. Thus, given the Cartesian coordinates (x,y) on $\mathcal{C}$ centred at its centroid, the components of displacement are: in plane $v_i = (v_x, v_y)$, and transverse w. The components of the strain tensor and the curvature terms, using the reciprocity conditions ($a_{ij} = a_{ji}$) read:

$$\varepsilon_x = \frac{\partial v_x}{\partial x} + \frac{1}{2}\left(\frac{\partial w}{\partial x}\right)^2, \qquad \varepsilon_y = \frac{\partial v_y}{\partial y} + \frac{1}{2}\left(\frac{\partial w}{\partial y}\right)^2,$$

$$\gamma_{xy} = \frac{\partial v_x}{\partial y} + \frac{\partial v_y}{\partial x} + \frac{\partial w}{\partial y}\frac{\partial w}{\partial x} \quad \textbf{(6a-c)}$$

$$\kappa_x = -\frac{\partial^2 w}{\partial x^2}, \quad \kappa_y = -\frac{\partial^2 w}{\partial y^2}, \quad \kappa_{xy} = -\frac{\partial^2 w}{\partial x \partial y} \quad \textbf{(7)}$$

The second term in Eq.'s (6a-c) represent the membrane strains whose associated deformation gradients are the sole contributors to geometric nonlinearity. The compatibility condition of strains is given by the following equation pair:

$$\frac{\partial^2 \varepsilon_x}{\partial y^2} + \frac{\partial^2 \varepsilon_y}{\partial x^2} - \frac{\partial^2 \gamma_{xy}}{\partial x \partial y} = \kappa_{xy}^2 - \kappa_x\kappa_y = -\det k \quad \textbf{(8)}$$

$$\nabla \times k = 0 \quad \textbf{(9)}$$

Eq. (8) represents the Gaussian invariant curvature (Gauss Theorema Eregium). The FVK Equations giving the fundamental description of nonlinear elastic dynamics of the thin plate reads:

$$D\nabla^4 w(x,y,t) - H\mathcal{L}(w,\Phi) = p(x,y,t) \tag{10}$$

$$\nabla^4\Phi(x,y,t) = -\frac{E}{2}\mathcal{L}(w,w) \Leftrightarrow -E(\kappa_x\kappa_y - \kappa_{xy}^2) \tag{11}$$

Thus, the Gaussian curvature is quadratic with respect to the transverse displacement field. Eq. (11) is a compatibility equation, where $\Phi(x,y,t)$ represents the Airy stress function, $D = \frac{EH^3}{12(1-\nu^2)}$ is the flexural rigidity of the plate, the biharmonic operator ∇^4 and the differential operator $\mathcal{L}(w,\Phi)$ are expressed by Eq.'s (12) and (13), respectively.

$$\nabla^4\Phi = \frac{\partial^4\Phi}{\partial x^4} + +2\frac{\partial^4\Phi}{\partial x^2\partial y^2} + \frac{\partial^4\Phi}{\partial y^4} \tag{12}$$

$$\mathcal{L}(w,\Phi) = \frac{\partial^2 w}{\partial x^2}\frac{\partial^2\Phi}{\partial y^2} + \frac{\partial^2 w}{\partial y^2}\frac{\partial^2\Phi}{\partial x^2} - 2\frac{\partial^2 w}{\partial y\partial x}\frac{\partial^2\Phi}{\partial x\partial y} \tag{13}$$

The Airy stress function represents the membrane action induced by large displacements and is defined by:

$$\sigma_{11} = \frac{\partial^2\Phi}{\partial y^2}, \qquad \sigma_{22} = \frac{\partial^2\Phi}{\partial x^2}, \qquad \sigma_{12} = -\frac{\partial^2\Phi}{\partial x\partial y} \tag{14}$$

Eq. (11) is a compatibility equation as discussed earlier, while $\mathcal{L}(w,w)$can also be expressed by replacing Φ with w in Eq. (13). Eq.'s (10)- (13) are coupled, highly nonlinear, fourth order Partial Differential Equations (PDE) which represent geometric nonlinearities of an elastic system induced by in-plane displacements and membranal forces. It is well known that even for simple engineering problems, the exact solution of FVK equations are notoriously difficult to obtain thus, in general, a numerical solution must be adopted. In the case of localised blast loads, the equations are fraught with more complexity due to the dependence of the load on the spatial and temporal multi-variables. Minimization of the FVK energy functionals calls for numerical Finite Element techniques, boundary elements, meshless methods, or some efficient variational method such as Ritz-Galerkin (RG). The approach resorted to herein seeks to reduce the PDE to a set of Ordinary Differential Equations (ODE's) using the Poincaré-Lindstedt (P-L) perturbation technique, combined with the RG method.

The mathematical procedure for such shell elements is outlined as follows:

1. Assume an ansatz for displacement fields and the associated stress tensors.
2. Determine the membranal stress from the compatibility relation of Eq. (13).
3. Update the displacement field from Eq. (10).
4. The final form of transverse displacement will be nonlinear, but in a reduced closed form expression.

The ansatz for displacement field and the associated stress functions may be expressed as multiplicative decomposition of their functions describing the spatial part as well as that of the temporal part, i.e. $w_{mn}(x,y,t) = H\overline{w}_{mn}(t)w^*(x,y)$ and $\phi_{mn}(x,y,t) = f(t)\phi^*(x,y)$, respectively, where the partial functions $w^*(x,y)$ and $\phi^*_{mn}(x,y)$ are expressed by Eq.'s (15)-(16). Accordingly, the dimensionless parameters $\bar{\phi} = f(t)/EH^2$, and $\overline{w}_{mn}(t) = w_{mn}(0,0,t)/H$ have been employed. Clearly, these expressions satisfy the displacement boundary conditions of the simply supported plate at its centre as well as along its periphery.

$$w^*(x,y) = \sum\nolimits_m \sum\nolimits_n \cos\frac{m\pi x}{2L}\cos\frac{n\pi y}{2L} \tag{15}$$

$$\phi^*(x,y) = \sum\nolimits_m \sum\nolimits_n \cos\frac{m\pi x}{2L}\cos\frac{n\pi y}{2L}$$
$$(m = 1,3,5, \dots \; and \; n = 1,3,5, \dots) \tag{16}$$

The RG technique to minimize the total elastic energy functional can be sketched in Eq.'s (17a-b). With this strategy, we may, dynamically update the interrelation between the transverse displacement field in Eq. (17a) from the state of membranal stress tensors satisfying Eq. (17b), and vice versa.

$$\int\int_{(A)} \{D\nabla^4\,\overline{w}^{(i+1)} - H^3E\mathcal{L}\left(\overline{w}^{(i)},\overline{\Phi}^{(i+1)}\right) + \mu\ddot{\overline{w}}^{(i+1)}\}\delta w dA = \int\int_{(A)} \frac{p(x,y,t)}{H}\delta w dA \tag{17a}$$

$$\int\int_{(A)} \left\{\nabla^4\overline{\Phi}^{(i+1)} + \frac{1}{2}\mathcal{L}\left(\overline{w}^{(i)},\overline{w}^{(i)}\right)\right\}\delta\Phi\, dA = 0 \tag{17b}$$

In Eq. (17a)- δw and $\delta\Phi$ represent the first variation (virtual parameter, or weight function) attributed to the displacement and Airy stress functions, respectively, while the superscript denotes the iteration. Substituting Eq.'s (15)-(16) in Eq. (17) furnishes the bending and strain energy contributors into:

$$\mathcal{L}(\overline{w},\overline{\Phi}) = \frac{1}{32}\frac{\pi^4}{L^4} m^2 n^2 \sum\nolimits_m \sum\nolimits_n \overline{w}_{mn}(t)\overline{\Phi}_{mn} \left(\cos\frac{m\pi x}{L} + \cos\frac{n\pi y}{L}\right) \quad \textbf{(18)}$$

$$\nabla^4 \overline{w} = \frac{1}{16}\frac{\pi^4}{L^4}(m^2+n^2)^2 \sum\nolimits_m \sum\nolimits_n \overline{W}_{mn}(t) \cos\frac{m\pi x}{2L} \cos\frac{n\pi y}{2L} \quad \textbf{(19)}$$

The operator $\mathcal{L}(\overline{w},\overline{w})$ and the biharmonic function $\nabla^4\overline{\Phi}$ may be recovered, in a similar fashion, by simply replacing $\overline{\Phi}$ with $\overline{w}$ in Eq. (18) and vice versa in Eq. (19). Assuming the Von-Mises yield criterion (J_2-plasticity), the Equivalent Mises stress is expressed as a function of the components of the deviatoric stress tensor as follows:

$$\sigma_{eq} = \frac{3}{2}\sqrt{s_{ij}s_{ij}} = \sqrt{3J_2} \quad \textbf{(20)}$$

Where $s_{ij} = \sigma_{ij} - \boldsymbol{p}\delta_{ij}$ are the components of the deviatoric stress tensor ($\boldsymbol{p} = \sigma_{kk}/3$), and J_2 is the second invariant of the deviatoric stress tensor and may be derived by substituting Eq.'s (A. 45)-(A. 47) in Eq. (21) (with $\sigma_{33} = 0$) as:

$$J_2 = \frac{1}{3}(\sigma_{11}^2 + \sigma_{22}^2 - \sigma_{11}\sigma_{22} + 3\sigma_{12}^2) \quad \textbf{(21)}$$

The associated Equivalent Mises strains are likewise derived as:

$$\varepsilon_{eq} = \frac{1}{3}\sqrt{6\varepsilon_{11}^2 + 6\varepsilon_{22}^2 + 3\varepsilon_{12}^2} \quad \textbf{(22)}$$

Throughout this work, ARMOX 440T steel has been used as the candidate material with the material properties outlined in Table 1, as well as the geometric dimensions of the membrane.

Table 1 Constants used in this study

Load parameters		**Geometric and material properties**				
b (m^{-1})	p_0 (MPa)	L (mm)	H (mm)	ν	E (GPa)	ρ ($kg.m^{-3}$)
50	40/200	200	4.6	0.3	200	7850

3 Dynamic Response

3.1 First Phase of Motion (Forced Vibration)

Now, substituting Eq.'s (18)-(19) in Eq.'s (17a-b) and performing the integrations reduces the form of FVK Partial Differential Equation to a paired set of $m \times n$ ODE's in terms of the transverse displacement fields, each representative of a unique mode shape of the MDOF system in forced vibration. While coupling between the modes is retained in the analysis, for the brevity in the mathematical treatment, only the first four terms of the truncated series (i. e. $m = n = 1{,}3$) may be considered. The set of ODE's were derived as

$$\omega_{\mathrm{mn}}^2 \bar{w}_{mn}{}^{(i+1)} + \ddot{\bar{w}}_{mn}{}^{(i+1)} + \frac{9E\pi^2\epsilon}{8\rho L^2}\boldsymbol{S(mn)}_{\mathbf{s1}}^{(i)}\,\bar{\boldsymbol{\Phi}}_{\mathbf{1k}}^{(i+1)}\delta'_{\mathrm{sk}} = \frac{4\alpha p_0}{\rho H^2} \qquad \textbf{(23)}$$

where $\epsilon = \frac{8}{9}H^2/L^2$ is a parameter of small value, while the matrices $\boldsymbol{S(mn)}_{s1}$ and $\bar{\boldsymbol{\Phi}}_{\mathbf{1k}}^{(i+1)}$ are defined in Eq.'s (24a-b), and δ'_{sk} is the Kronecker Delta. Then, for each displacement field term $\bar{w}_{mn}$, the associated components of the matrix $\boldsymbol{B}_{mn}$ are expressed in Eq.'s (A-48)-(A-50). From the compatibility Eq. (17b) the components of $\bar{\boldsymbol{\Phi}}_{1k}^{(\mathrm{i}+1)}$ in Eq. (23) with $i = 1$ can be unequivocally determined as in Eq.'s (A. 51)-(A. 53). In the absence of higher order terms, $\bar{\phi}_{11}^{(2)} = -\frac{4}{3\pi^2}\bar{w}_{11}^{(i)\,2}$ and the solution converges to the case of an SDOF system.

$$\boldsymbol{S(mn)}_{s1}^{(\mathrm{i})} = \boldsymbol{B}_{mn}\left[\bar{w}_{11}^{(i)}\ \bar{w}_{13}^{(i)}\bar{w}_{31}^{(i)}\bar{w}_{33}^{(i)}\right]',\ \bar{\boldsymbol{\Phi}}_{1k}^{(i+1)} = \left[\bar{\phi}_{11}^{(\mathrm{i}+1)}\quad \bar{\phi}_{13}^{(\mathrm{i}+1)}\quad \bar{\phi}_{31}^{(\mathrm{i}+1)}\quad \bar{\phi}_{33}^{(\mathrm{i}+1)}\ \right]. \qquad \textbf{(24a-b)}$$

It should be noted that, each ODE in Eq. (23) correspond to a mode of vibration with the mode coupling appearing in the nonlinear term $\bar{\boldsymbol{\Phi}}_{1k}^{(\mathrm{i}+1)}$. The coefficients of $\bar{\boldsymbol{\Phi}}_{1k}^{(\mathrm{i}+1)}$ may be visualized as the equivalent membrane stiffness of the plate while the vibration frequency ω_{mn}^2 gives the ratio of the bending stiffness to the equivalent mass of the structure. Thus, the vibration frequency ω_{mn} is determined as:

$$\omega_{mn} = \frac{1}{4}\frac{\pi^2}{L^2}(m^2+n^2)\sqrt{\frac{D}{\mu}} = \frac{\sqrt{3}}{24}\frac{\pi^2 H}{L^2}(m^2+n^2)\sqrt{\frac{E}{\rho(1-\nu^2)}} \qquad \textbf{(25)}$$

confirming that the modal vibration frequencies uniquely depend on the speed of dilatational wave propagation through the plate as well as its slenderness ratio. Clearly, each of the ODE's of Eq.(23) is an inhomogeneous, expanded form of Duffing equation [38]. If the high order transverse displacement terms are ignored, using the separation of variables, the closed form explicit solution of this ODE can be expressed as ($\dot{\bar{w}}^2 = h + \frac{8\alpha p_0}{\mu H}\bar{w} - [\omega_{11}^2\bar{w}^2 + \frac{E}{2\rho L^2}\epsilon\bar{w}^4]$, where h is the integration constant) with the left hand side representing the normalised kinetic energy per mass of the system. If ϵ is positive, the force-displacement gradient increases and the system represents hardening [20], in which case the plane plot encompasses an elliptic manifold, as is the case here (as illustrated in Fig. 3), while in the circumstances of negative ϵ the softening of the stiffness would occur.

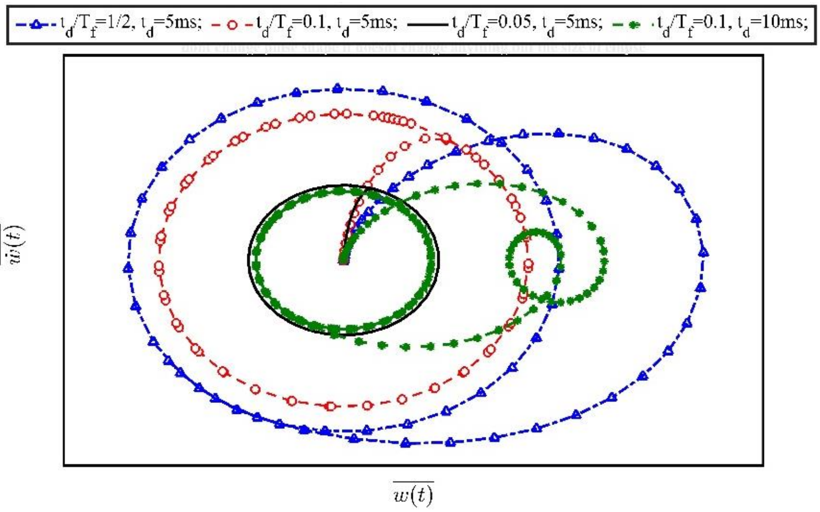

Fig. 3- Phase plane for various values of t_d, where T_f is an arbitrary time point

Heuristically, with the nonlinear terms present in the Eq. (23), the explicit solution entails the presence of secular terms (in the form of $t\sin(t)$) which bring about a non-harmonic response with unbounded growth of transient displacements. The solution can be made harmonic by employing the Poincaré-Lindstedt perturbation method to eliminate, once and for all, the dependence of the displacement field on such terms. To this end, the frequency response is normalised as $\tau_{mn} = (\omega_{mn} + \epsilon\bar{\omega}_{mn} + O(\epsilon^2))$, where $\bar{\omega}_{mn}$ is referred to as the pseudo vibration hereinafter. Accordingly, the displacement field is expressed as a truncated series of its iterative terms given by:

$$\bar{w}_{mn}(\tau_{mn}) = \bar{w}_{mn}{}^{(1)}(\tau_{mn}) + \epsilon\bar{w}_{mn}{}^{(2)}(\tau_{mn}) + O(\epsilon^2) \tag{26}$$

The solution to the first iteration $\bar{w}_{mn}{}^{(1)}$ is derived by linearizing the form of the ODE in Eq. (23), i.e. eliminating the Airy Stress function terms $\boldsymbol{Q}_{1\mathrm{k}}^{(1)}$. The general solution of the system must satisfy the initial kinematic conditions $\bar{w}(0) = \dot{\bar{w}}(0) = 0$, and can be sketched as:

$$\bar{w}_{mn}^{(1)} = c_{mn}(1 - \cos(\omega_{mn}t)) \tag{27}$$

where the amplitude of vibration is

$$c_{mn} = \frac{4\alpha p_0}{\mu H\omega_{mn}^2} \tag{28}$$

To derive the ODE expression for the second term, we shall henceforth ignore the terms of higher order as $\epsilon^2 << 1$. Substituting Eq. (26) in Eq. (23)together with the use of Eq. (27) yields

$$\omega_1^2(\overline{w}^{(2)}{}_{mn} + \ddot{\overline{w}}^{(2)}{}_{mn}) + 2\omega_{mn}\overline{\omega}_1 c_{mn}\ddot{\overline{w}}^{(1)}{}_{mn} + \frac{9E\pi^2}{8\rho L^2}\boldsymbol{S}^{(\mathbf{1})}_{mns1}\,\overline{\boldsymbol{\Phi}}^{(2)}_{1k}\delta'_{\mathrm{sk}} = 0 \tag{29}$$

From Eq. (27) the second iteration for the Airy Stress function at the plate centre is attained. Sequentially, the ODE of Eq. (23) is re-evaluated and solved to determine, unequivocally by imposing the initial boundary conditions, the plate maximum transverse displacement as:

$$\begin{aligned}\overline{w}^{(1)}_{11} &= \left(\frac{2.2Ec_{11}^3}{\omega_{11}^2\,L^2\rho} - \frac{c_{11}\overline{\omega}_1}{\omega_{11}}\right)sin(\tau_{11})\tau_{11} \\ &\quad + \frac{c11^3E}{L^2\rho\omega_1^2}\{-0.0347cos(\tau_{11})^{15} + 0.1302cos(\tau_{11})^{13} - 0.273cos(\tau_{11})^{11} \\ &\quad + 0.109cos(\tau_{11})^{10} + 0.335cos(\tau_{11})^{9} - 0.274cos(\tau_{11})^{8} - 0.282cos(\tau_{11})^{7} \\ &\quad + 0.471cos(\tau_{11})^{6} - 0.0861\cos(\tau_{11})^{5} - 0.297cos(\tau_{11})^{4} + 0.118cos(\tau_{11})^{3} \\ &\quad + 1.13cos(\tau_{11})^{2} + 2.52cos(\tau_{11}) - 3.5664\}\end{aligned} \tag{30}$$

$$\overline{\omega}_{11} = \frac{2.2Ec_{11}^2}{L^2\omega_1\rho} \tag{31}$$

where the derived parameter $\overline{\omega}_1$ in Eq. (31), determined by the first bracket of Eq. (30), eliminates the secular term and to make the response periodic. Further iterative components of Airy stress matrix function $\overline{\boldsymbol{\Phi}}^{(\mathrm{i})}_{1k}$ may be evaluated by substituting Eq.'s (30),(32), and (33) in each of the Eq.'s (A. 51)-(A. 53).

In a similar fashion, the expressions for $\overline{w}^{(2)}_{13}$ and $\overline{w}^{(2)}_{33}$ are determined as Eq.'s (32) and (33). It is interesting to note the infinitesimal disparity between the values of $\overline{\omega}_{ij}$ in the associated higher modes to that of the fundamental mode. For example, the value of $\overline{\omega}_{13}$ is only 2.4% lower than $\overline{\omega}_{11}$.

$$\begin{aligned}\overline{w}^{(1)}_{13} &= \left(\frac{6710c_{13}^2E}{L^2\rho\,\omega_{13}^2} - \frac{\overline{\omega}_{13}}{\omega_{13}}\right)c_{13}sin(\tau_{13})\tau_{13} \\ &\quad + \frac{Ec_{13}^3}{L^2\rho\omega_{13}^2}\Bigg(6.98sin\left(\frac{3}{2}\tau_{13}\right)^2 - 6730sin\left(\frac{1}{2}\tau_{13}\right)^2 + 58720sin\left(\frac{1}{5}\tau_{13}\right)^2 \\ &\quad + 46110sin\left(\frac{2}{5}\tau_{13}\right)^2 - 37730sin\left(\frac{3}{5}\tau_{13}\right)^2 - 143150sin\left(\frac{1}{10}\tau_{13}\right)^2 \\ &\quad - 16590sin\left(\frac{3}{10}\tau_{13}\right)^2 + 3740sin\left(\frac{7}{10}\tau_{13}\right)^2 + 248.44sin\left(\frac{9}{10}\tau_{13}\right)^2 \\ &\quad + 144.92\,sin\left(\frac{11}{10}\tau_{13}\right)^2 - 482.67sin(\tau_{13})^2\Bigg)\end{aligned} \tag{32}$$

$$\bar{w}_{33}^{(1)} = \frac{c_{11}^3 E}{L^2 \omega_{33}^2 \rho}\Big(-0.106cos(\tau_{33}) + 0.882 - 0.105cos\left(\frac{10}{3}\tau_{33}\right) - 0.897cos\left(\frac{10}{9}\tau_{33}\right) - 0.0799cos\left(\frac{11}{9}\tau_{33}\right) - 0.186cos\left(\frac{7}{9}\tau_{33}\right) - 0.449cos\left(\frac{2}{3}\tau_{33}\right) + 0.741cos\left(\frac{2}{9}\tau_{33}\right) + 0.619cos\left(\frac{5}{9}\tau_{33}\right) + 0.477cos\left(\frac{8}{9}\tau_{33}\right) - 0.318cos\left(\frac{4}{9}\tau_{33}\right) + 0.3759\cos(\tau_{33}\Big) \tag{33}$$

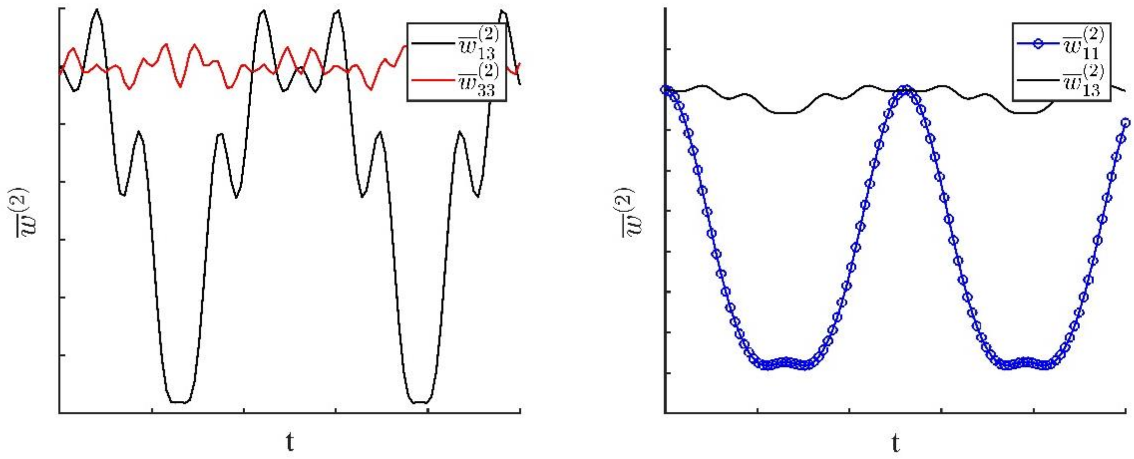

(a) (b)

Fig. 4- Comparison of modal deformations histories in the first phase of motion, for (a) second and third mode, (b) first and second mode

It can be seen in Fig. 4 that the influence of higher modes on the overall transient response of the structure is inconsequential. Thus, the mathematical treatment of elastic systems with merely two terms of the truncated series renders the overall response sufficiently accurate.

3.2 Second Phase of Motion (Free Vibration)

The loading is complete at time $t = t_d$; however, the system retains its motion due to the initial inertia effects and the energy stored in it. Thus, the associated response of the plate is governed by a free vibration following the forced vibration of the previous phase. Thus, at the time point of completion of loading, the kinematic continuity applies to ensure there is no displacement or velocity jumps throughout the motion.

The analysis in this phase is carried out in the same spirit as the previous phase of motion- with the solution of linear and nonlinear parts of the displacement field determined on $\bar{\mathbf{\Phi}}_{1k}^{(1)} = 0$

(or $\epsilon_0 = 0$), and on $\bar{\mathbf{\Phi}}_{1k}^{(2)}$, respectively. Thus, by disregarding the nonlinear terms, the first iteration of ODE is expressed, using the kinematic continuity of displacement and velocity fields of each mode at $t = t_d$, as:

$$\bar{w}_{mn}{}^{(1)} = c_{mn}\left(cos\left(\omega_{mn}(t - t_d)\right) - cos(\omega_{mn} t)\right) \quad \textbf{(34)}$$

The plate reaches its peak transient deformations when the velocity vanishes, i.e. $\dot{\bar{w}}_{mn}{}^{(i)} = 0$, occurring at

$$T_{max} = \frac{1}{2\omega_{mn}}\left((2k-1)\pi + \omega_{mn} t_d\right) \quad \textbf{(35)}$$

where k is an integer. Using Eq.'s (34) and (35), the extrema of deformation are derived as $\bar{\boldsymbol{w}}_{mn}{}^{(1)} = \pm 2c_{mn} \sin\left(\frac{\omega_{mn} t_d}{2}\right)$. A plot of the maximum transient deformation against various load magnitudes is illustrated in Fig. 5.

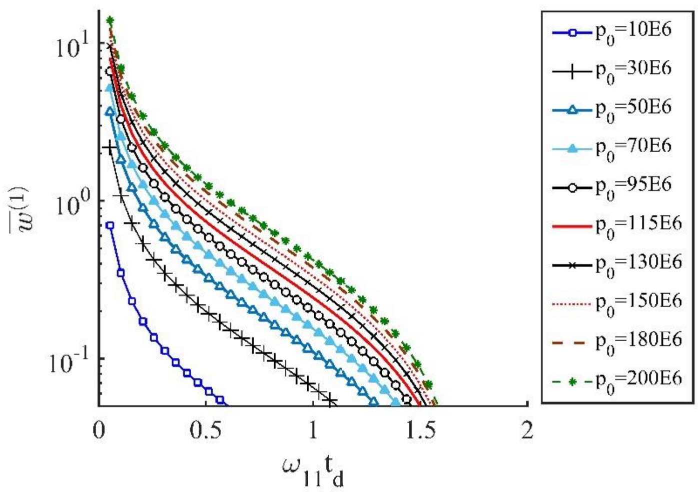

Fig. 5- Variations of the peak transient Mid-point deflection with load magnitude

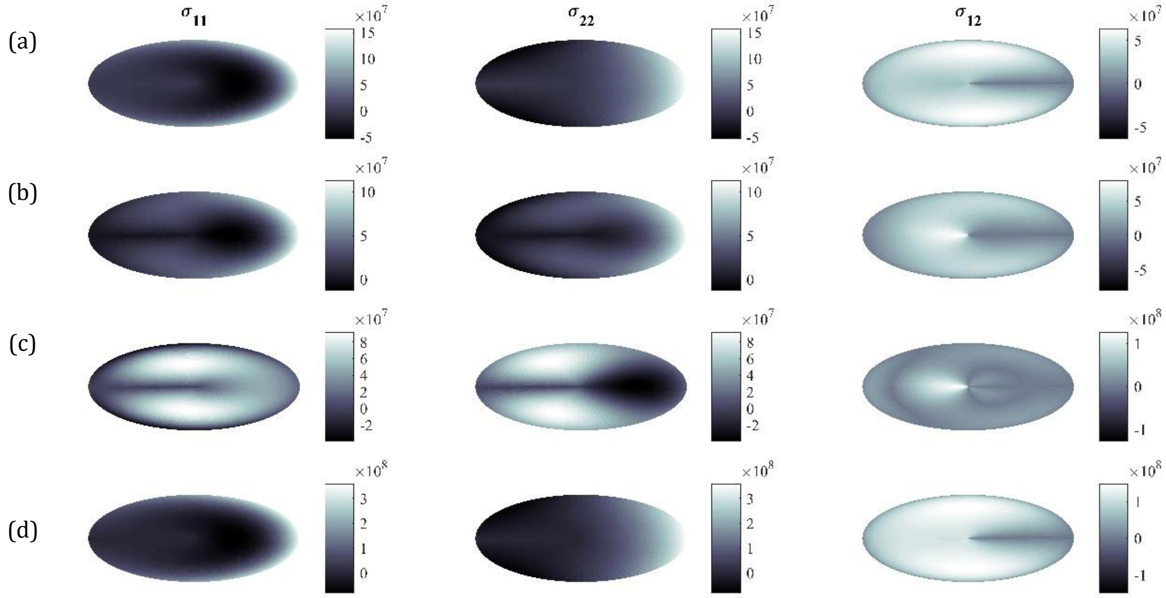

Fig. 6- -The three stress components in elliptic manifold at $t = 5t_d$ (a), $t = 10t_d$ (b), $t = 20t_d$ (c) and $t = 100t_d$ (d), where $t_d = 30\mu s$ and $R_e/L = 0.25$

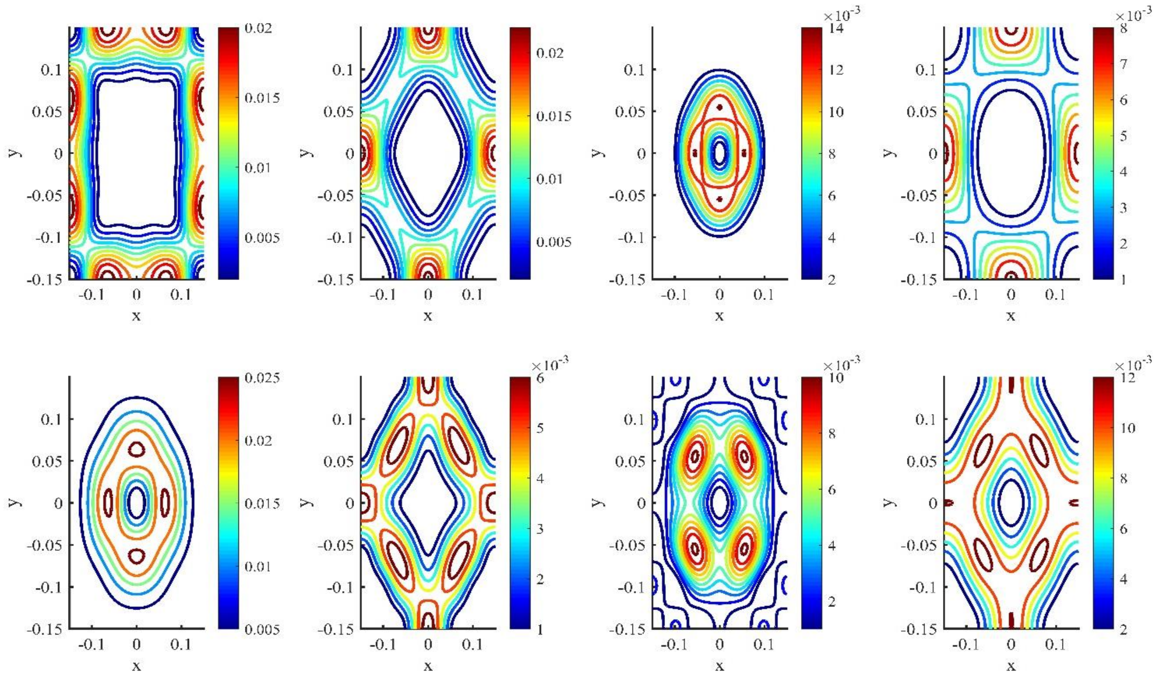

Fig. 7- Contour plot of von Mises strains over time in the plate at different times $t = 4t_d - 30t_d$ with $p_0 = 40MPa$ and $^{R_e}/_{L} = 0.25$.

In Fig. 6, the main components of the stress tensor viz. σ_{11}, σ_{22}, and σ_{12} across the target plate are mapped onto an elliptical surface, with $\sigma_{11} = \phi_{mn,22}$, $\sigma_{22} = \phi_{mn,11}$, and $\sigma_{12} = -\phi_{mn,12}$, whereas Fig. 7 depicts the distribution of Equivalent Mises strain over the plate surface at various times. The associated von Mises stress distributions are illustrated in Fig. 8.

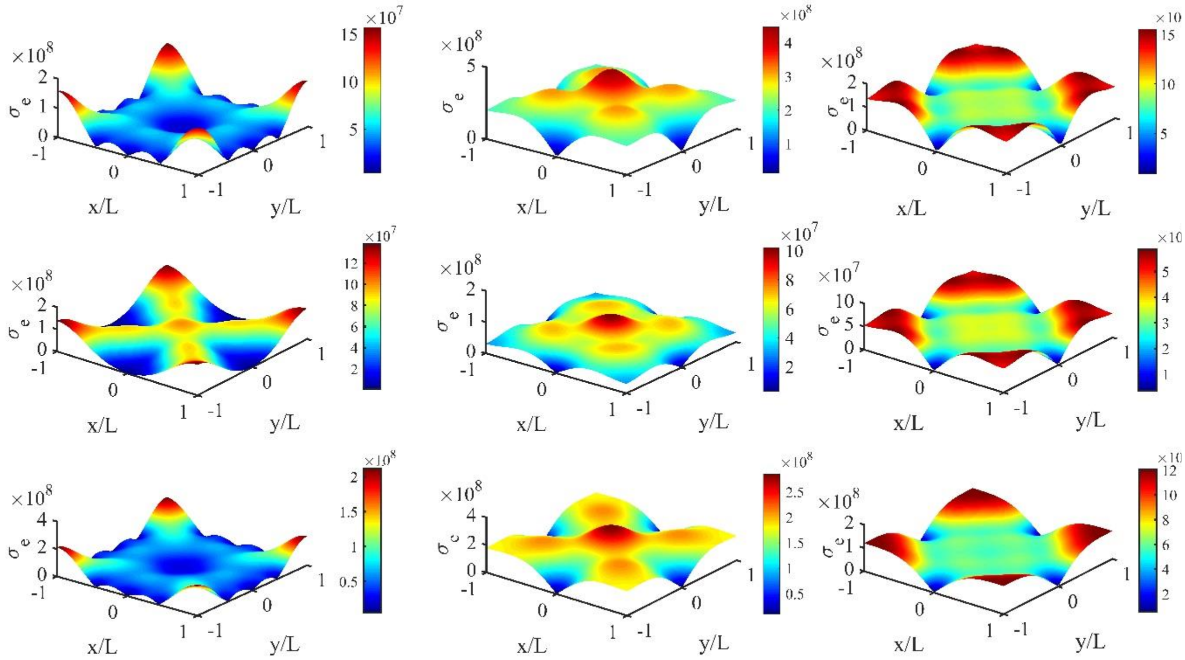

Fig. 8- Evolution of von Mises stress over time in the plate at different times $t = 4t_d - 30t_d$, with $p_0 = 40MPa$and $^{R_e}/_{L} = 0.25$.

The displacement field in Eq. (34) is employed to determine $\bar{\mathbf{\Phi}}_{1k}^{(2)}$, which, together with the inertia term, are substituted in the ODE of Eq. (29). While the explicit solution for each mode in Eq. (29) exists, regardless of the number of DOF's entailed, clearly, the mathematical treatment is cumbersome even with a reduced MDOF model, due to the presence of multiplicative decomposition in each mode. However, as observed in this work, it turns out that the contribution of the higher modes $\bar{w}_{33}{}^{(1)}$ to the overall mid-point deformation of the plate is vanishingly small and may be disregarded while the accuracy of the solution is maintained. The fundamental mode solution may be derived as:

$$\bar{w}_{11}{}^{(2)} = C_4\cos(\tau_{11}) + C_5\sin(\tau_{11}) + f(\tau_{11}) + \frac{c_{11}\bar{\omega}_{11}}{2\omega_{11}}\left(cos(\tau_{11} - \bar{t_d}) - cos(\tau_{11})\right) \qquad \textbf{(36)}$$

where $f(\tau_{11})$ is expressed in Eq. (A-54). The integration constants, given in Eq.'s (A. 55)-(A. 56), are derived by ensuring the kinematic continuity of transverse displacement and velocity fields between the phases. The pseudo vibration $\bar{\omega}_1$ which normalizes the response into harmonic may be unequivocally determined, as in Eq. (37), to eliminate the secular term in this phase.

$$\bar{\omega}_{11} = [0.8 - (0.29sin(\bar{t_d})^4 - 0.22sin(\bar{t_d})^2 + 0.8)cos(\bar{t_d})]\frac{Ec_{11}^2}{L^2\rho\omega_{11}} \quad \textbf{(37)}$$

For an SDOF system, this parameter would reduce to:

$$\bar{\omega}_1 = \frac{3Ec_{11}^2}{4L^2\rho\omega_{11}}\left(1 - cos(\bar{t_d})\right) \quad \textbf{(38)}$$

A comparison of $\bar{\omega}_1$'s for SDOF and MDOF model in Fig. 9 reveals an insignificant difference between the two values indeed. In Fig. 10, the interaction between the load duration, central constant load radius and $\bar{\omega}_1$ is graphed for various values of thickness.

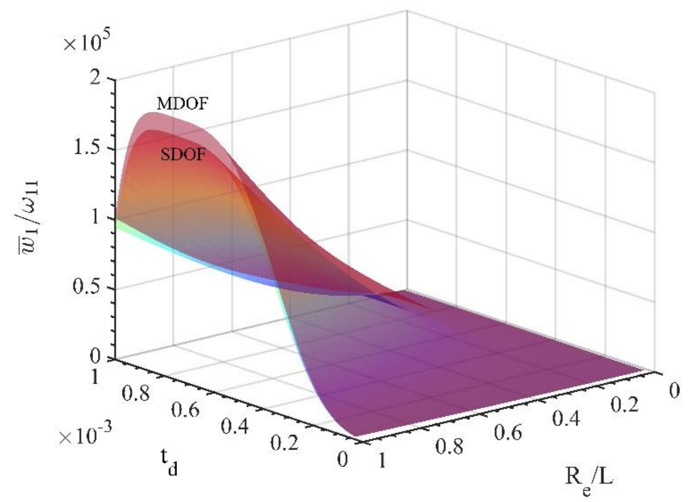

Fig. 9 Comparison of SDOF and MDOF pseudo vibrations

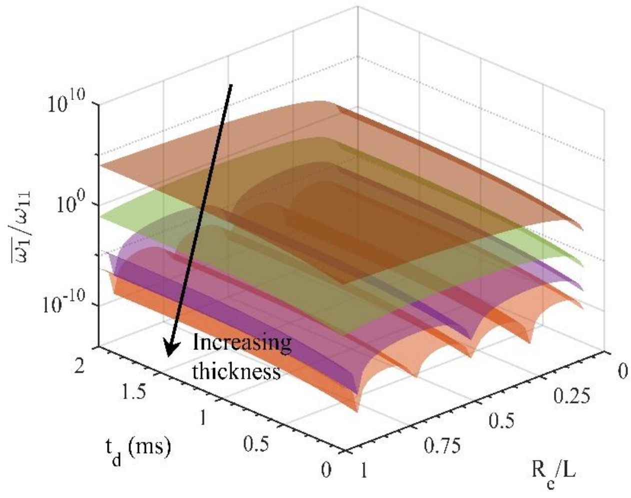

Fig. 10- Interaction surface of the load duration, Load radius and pseudo vibration for SDOF model

Similarly, for the second mode $\overline{w}_{13}^{(2)}$ we have:

$$\overline{w}_{13}{}^{(2)} = C_6 \cos(\tau_{11}) + C_7 \sin(\tau_{11}) + f(\tau_{13}) + \frac{c_{13}\overline{\omega}_{13}}{2\omega_{13}}\left(cos(\tau_{13} - \overline{t_d}) - cos(\tau_{13})\right) \quad \textbf{(39)}$$

Where Eq. (A-57) gives the function $f(\tau_{13})$, while the integration constants are expressed in Eq.'s (A. 58)-(A. 59). It should be stressed that in this phase $\overline{\omega}_{13} \cong \overline{\omega}_{11}$ applies.

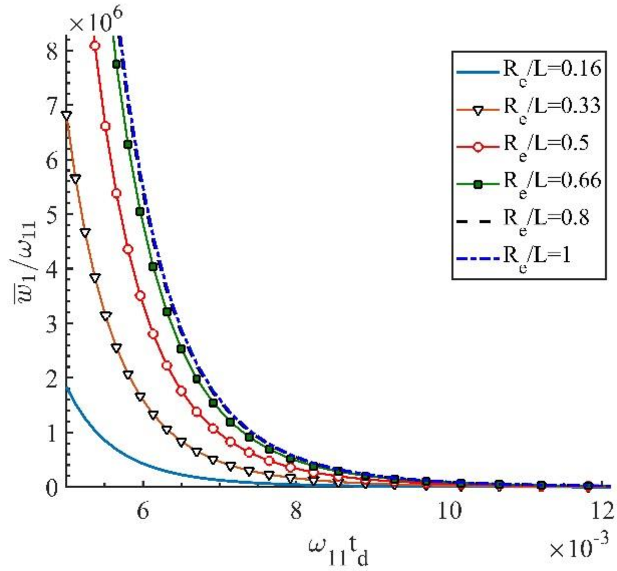

Fig. 11 Variations of the pseudo vibrations with vibration frequency

This concludes the two phases of motion and the method adopted is universally applicable.

4 Influence of pulse shape

It has been shown the pulse shape has a pronounced effect on the response of plates made of rigid-perfectly plastic materials. It would be interesting to see if the influence of pulse shape on FVK plate is significant. This effect is investigated on the plates studied here. More often than not, a non-impulsive pressure load may assume various temporal pulse shapes contingent upon the source of blast. A general expression of pulse shapes expressed by Li and Meng [3] reads:

$$p_2(t) = \begin{cases} \left(1 - X\dfrac{t}{t_d}\right)e^{-Y\frac{t}{t_d}}, & 0 \le t \le t_d \\ 0 & t_d \le t \end{cases} \tag{40}$$

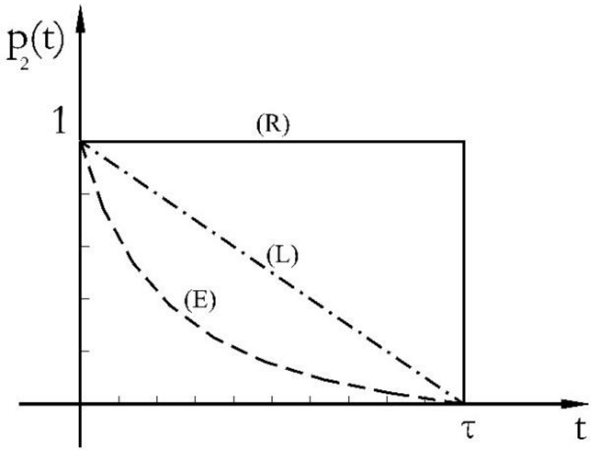

Fig. 12- Typical temporal pulse loading shapes (R) rectngular (L) linear, (E) exponential

where X and Y are pulse shape parameters obtained experimentally or numerically. Through the correct choice of these parameters, the expression in Eq. (40) can define any linear or exponential pulse, while in the case of $X = Y = 0$, Eq. (40) reduces to the case of a rectangular pulse. The expression of $\overline{w}_{mn}^{(1)}$ would be modified in the first phase of motion as:

$$w_{mn}^{(1)} = C_1 cos(\omega_{mn}t) + C_2 sin(\omega_{mn}t) + -\frac{\left((Xt - t_d)\left(\omega_{mn}^2 t_d^2 + Y^2\right) + 2XYt_d\right) t_d c_{mn} \omega_{mn}^2 e^{-\frac{Yt}{t_d}}}{(\omega_{mn}^2 t_d^2 + Y^2)^2} \tag{41}$$

where the constants C_1 and C_2 are obtained as:

$$C_1 = \frac{\left(-\omega_{mn}^2 t_d^2 + 2XY - Y^2\right)\omega_{mn}^2 t_d^2}{(\omega_{mn}^2 t_d^2 + Y^2)^2} c_{mn} \tag{42}$$

$$C_2 = -\frac{t_d c_{mn} \omega_{mn} \left(-X\omega_{11}^2 t_d^2 - Y\omega_{mn}^2 t_d^2 + XY^2 - Y^3\right)}{(\omega_{mn}^2 t_d^2 + Y^2)^2} \tag{43}$$

Similarly, for the second phase of motion,

$$w_{mn}^{(1)} = \frac{c_{mn}\omega_{mn}t_d}{(\omega_{mn}^2 t_d^2 + Y^2)^2}\left(G_1 sin(\omega_{mn}t) + E_1 cos(\omega_{mn}t)\right) \tag{44}$$

With the integration constants obtained as Eq.'s (A. 61)-(A. 62). Fig. 12 compares the different pulse shapes, while the influence of pulse shape on the transient and maximum deformation are plotted in Fig. 13-Fig. 14, where $X = 0$ and $Y = 0$ are prescribed for the exponential and rectangular pulse shapes, respectively. The derivation of the maximum deformation of the plate is expressed in Eq.'s (A. 63),(A. 66).

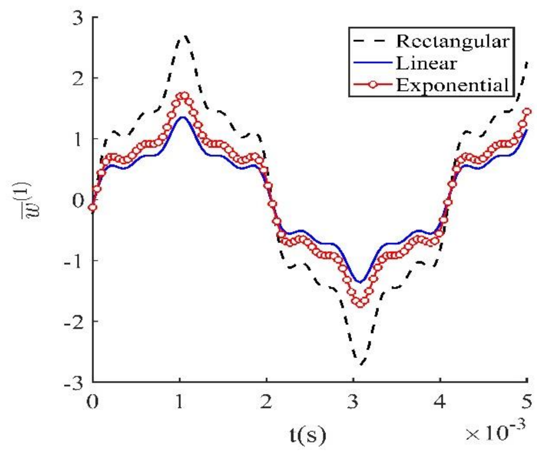

Fig. 13- Transient deformation of the plate for typical temporal pulse loading shapes (R) rectngular, (L) linear, and (E) exponential

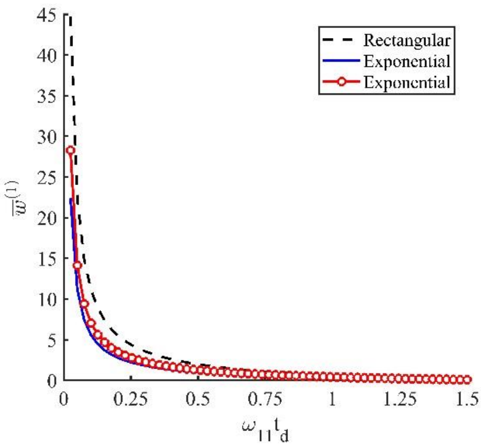

Fig. 14- Maximum deformation of the plate for typical temporal pulse loading shapes (R) rectngular, (L) linear, and (E) exponential

5 Numerical Validations and discussions

In this section, the analytical solutions are validated against the results of a numerical model devised in the commercial finite element software ABAQUS®14.4 Explicit. A full 3D square plate was set up with a total geometric exposed area of 400×400mm . The plate was fixed along its periphery with simply supported boundary conditions. The axisymmetric properties of the load and the 8 symmetries of the plate reduce the model to only a quarter of the plate, while the influence of finite deflections (geometry changes) was retained in the numerical model.

The material properties were those of isotropic elastic metals with high yield strength such as ARMOX 440T sheets. These panels were High Hardness Armour graded steel alloy types used for blast protective plates and manufactured by SSAB® [39], [40]. The geometric and material properties of the plates were taken from [8] (Table 1).

The models were discretized with a fine mesh of four-noded S4R isoparametric general shell elements with reduced integration and finite membrane strains possessing 5 Simpson integration points through the thickness of the plate. These elements are general-purpose conventional shells with the reduced integration formulation and hourglass control to prevent both shear locking and spurious energy (hour glassing). A total of 2500 elements were assigned to give the quotient of the element length to thickness as 0.87 to satisfy the convergence [8].

Two blast loading scenarios of 40MPa and 200MPa magnitudes were assumed, with pulse shape of rectangular profile and duration of $100\mu s$ and $30\mu s$, respectively. The radius of the central uniform blast zone was taken to be 25mm and 50mm for each case, respectively. The transient deformation of the panels was investigated in each blast scenario the results of which are shown in Fig. 15 and Fig. 16. Fig. 17 also compares the transient deformation for the SDOF model with a blast load of amplitude $40MPa$ and $50\mu s$ loading duration with the numerical model.

Clearly, while the vibration frequency of the analytical model in its first (fundamental mode) is lower than its FE counterpart, in the higher modes the frequencies increase while the peak displacements decrease. The higher modes enhance the residual vibrations at each cycle but infinitesimally affect the overall peak deformation. For example, like the first phase, the peak deformation of the first mode was found to be 70% higher than the second mode. Furthermore, there is a good agreement between the analytical and numerical models in prediction of peak displacements. Consequently, the mathematical treatment of the problem favoring only the first and second modes would suffice to predict the response.

In Table 2 and Table 3 the peak deformation from the numerical models and the analytical counterparts for various blast load radii compare favourably. Higher errors are attributed to more uniform blasts which may be due to overprediction of the load parameter.

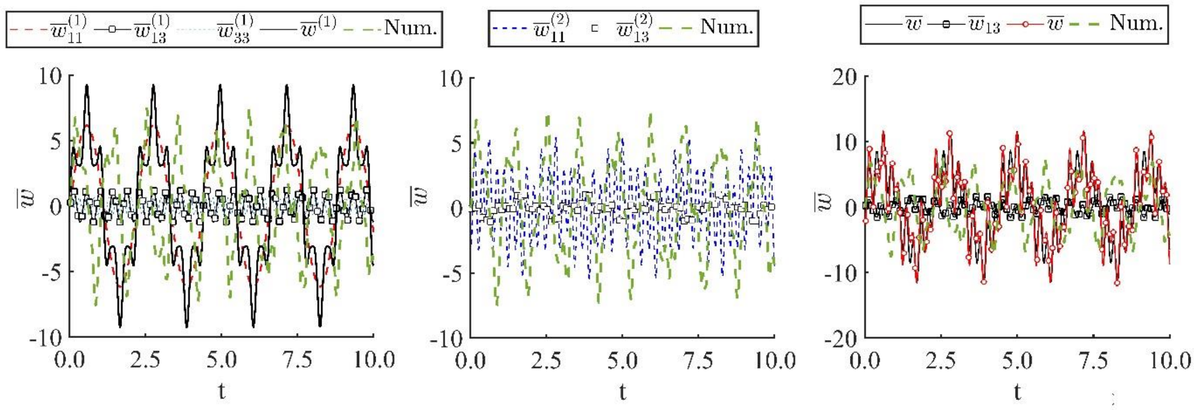

Fig. 15- Deformation time history of 200Mpa load- Analytical vs FE model (time in ms)

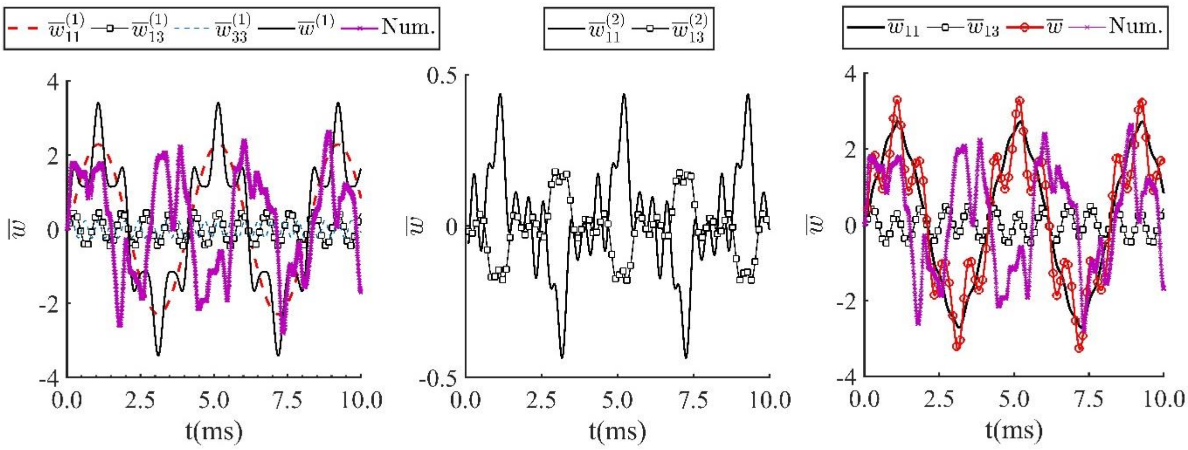

Fig. 16 Deformation time history of 40Mpa load- Analytical vs FE model

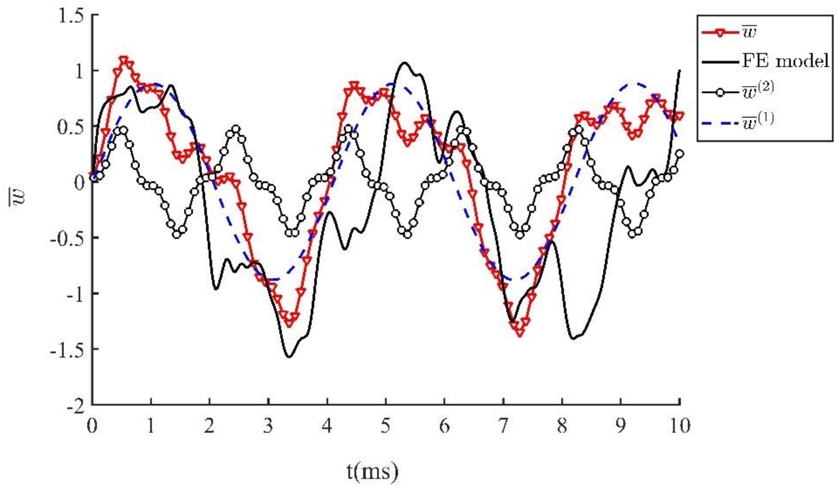

Fig. 17- Validations of the analytical model (SDOF) with $p_0 = 40MPa$, $R_e = 25mm$

Table 2 Peak central displacement of the plate on $p_0 = 40MPa$, analytical vs FE model

R_e/L	$\bar{w}_{11}$	$\bar{w}_{13}$	$\bar{w}_{33}$	$\bar{w}$	ABAQUS	% Error
0.125	1.46	0.28	0.13	2.15	2.63	18.37
0.25	2.82	0.53	0.26	4.14	3.94	5.04
0.375	4.09	0.77	0.37	6.01	5.17	16.10
0.5	4.91	0.93	0.45	7.21	6.25	15.36

Table 3- Peak central displacement of the plate on $p_0 = 200MPa$, analytical vs FE model

R_e/L	$\bar{w}_{11}$	$\bar{w}_{13}$	$\bar{w}_{33}$	$\bar{w}$	ABAQUS	% Error
0.125	2.20	0.44	0.24	2.88	3.21	10.27
0.25	4.24	0.84	0.46	5.55	4.78	16.14
0.375	6.15	1.22	0.67	8.05	6.36	26.60
0.5	7.38	1.47	0.81	9.66	7.52	28.46

6 Concluding remarks

This work deals with dynamic response of nonlinear elastic thin plated structures subject to localised blasts due to proximal charges. The localised blast load was assumed to be multiplicatively decomposable into a spatial and a temporal distribution. Considering this idealization, and using the Ritz-Galerkin functional, a single dimensionless parameter was obtained which characterises various blast loading scenarios by the correct choice of its parameters b, R_e .

The Ritz-Galerkin method was similarly employed to minimize the nonlinear coupled FVK equations considering a kinematically admissible displacement field and an associated Airy stress function as a truncated cosine series - each term representative of a unique mode of vibration- in an iterative procedure. The state variables were determined in two distinguished phases of motion, the first reflecting the forced vibration while the second addressing the free vibration due to initial inertia effects and the stored elastic energy of the system. The Poincaré-Lindstedt perturbation method was employed to avoid the non-convergent explicit solution due to the presence of secular terms whilst satisfying a predicted harmonic oscillation.

The presence of higher modes had little effect on the overall response of the plate as the observed peak deformations from the first to second mode decreased significantly and were more diminutive with respect to the fourth mode ($\bar{w}_{33}$). The MDOF model offered more accurate oscillation frequency, capable of predicting the residual vibrations. The results of dynamic analyses conducted were corroborated with the commercial FE software ABAQUS/Explicit and strong correlation was observed in all cases.

The influence of pulse shape was investigated whereby significant differences between the impulsive-characterised pulse and rectangular pulse- and non-impulsive blasts were observed. In accordance with the results of [23], clearly, the blast load is in a state of attenuation with the increase of the load temporal decay parameter (Y), leading to the decrease of response amplitudes. Similar trend is evident with the variation of the load shape decay parameter (b).

7 Citations

[1] D. Bonorchis and G. N. Nurick, “The influence of boundary conditions on the loading of rectangular plates subjected to localised blast loading - Importance in numerical simulations,” *Int. J. Impact Eng.*, vol. 36, no. 1, pp. 40–52, 2009.

[2] N. Mehreganian, A. S Fallah, and L. A. Louca, “Inelastic dynamic response of square membranes subjected to localised blast loading,” *Int. J. Mech. Sci.*, vol. 148, no. August, pp. 578–595, 2018.

[3] Q. M. Li and H. Meng, “Pulse loading shape effects on pressure-impulse diagram of an elastic-plastic, single-degree-of-freedom structural model,” *Int. J. Mech. Sci.*, vol. 44, no. 9, pp. 1985–1998, 2002.

[4] A. S. Fallah and L. A. Louca, “Pressure-impulse diagrams for elastic-plastic-hardening and softening single-degree-of-freedom models subjected to blast loading,” *Int. J. Impact Eng.*, vol. 34, no. 4, pp. 823–842, 2007.

[5] C. Zheng, X. S. Kong, W. G. Wu, and F. Liu, “The elastic-plastic dynamic response of stiffened plates under confined blast load,” *Int. J. Impact Eng.*, vol. 95, pp. 141–153, 2016.

[6] P. S. Symonds, “Elastic, Finite Deflection and Strain Rate Effects in a Mode Approximation Technique for Plastic Deformation of Pulse Loaded Structures.,” *J. Mech. Eng. Sci.*, vol. 22, no. 4, pp. 189–197, 1980.

[7] N. Jones, *Structural Impact*, 1st ed. Cambridge: Cambridge University Press, 1997.

[8] N. Mehreganian, L. A. Louca, G. S. Langdon, R. J. Curry, and N. Abdul-Karim, “The response of mild steel and armour steel plates to localised air-blast loading-comparison of numerical modelling techniques,” *Int. J. Impact Eng.*, vol. 115, no. January, pp. 81–93, 2018.

[9] B. McDonald, H. Bornstein, G. S. Langdon, R. Curry, A. Daliri, and A. C. Orifici, “Experimental response of high strength steels to localised blast loading,” *Int. J. Impact Eng.*, vol. 115, no. October 2017, pp. 106–119, 2018.

[10] P. S. Symonds and W. T. Fleming, “Parkes revisited: On rigid-plastic and elastic-plastic dynamic structural analysis,” *Int. J. Impact Eng.*, vol. 2, no. 1, pp. 1–36, 1984.

[11] S. Vidoli, “Discrete approximations of the Föppl – Von Kármán shell model : From coarse to more refined models,” *Int. J. Solids Struct.*, vol. 50, no. 9, pp. 1241–1252, 2013.

[12] E. H. DOWELL and C. S. VENTRES, “Comparison of theory and experiment for nonlinear flutter of loaded plates,” *AIAA J.*, vol. 8, no. 11, pp. 2022–2030, 1970.

[13] E. H. . Dowell and O. Bendiksen, *Panel flutter. Encyclopedia of Aerospace Engineering*. John Wiley & Sons, 2010.

[14] P. Del Linz, X. Liang, P. A. Hooper, L. Z. Wang, and J. P. Dear, “An analytical solution for pre-crack behaviour of laminated glass under blast loading,” *Compos. Struct.*, vol. 144, pp. 156–164, 2016.

[15] Y. Yuan, P. J. Tan, and Y. Li, “Dynamic structural response of laminated glass panels to blast loading,” *Compos. Struct.*, vol. 182, no. August, pp. 579–589, 2017.

[16] P. Hooper, “Blast performance of silicone-bonded laminated glass (PhD Thesis),” Imperial College London, 2011.

[17] M. L. Dano and M. W. Hyer, “Thermally-induced deformation behavior of unsymmetric laminates,” *Int. J. Solids Struct.*, vol. 35, no. 17, pp. 2101–2120, 1998.

[18] J. Dervaux, P. Ciarletta, and M. Ben Amar, “Morphogenesis of thin hyperelastic plates: A constitutive theory of biological growth in the Föppl-von Kármán limit,” *J. Mech. Phys. Solids*, vol. 57, no. 3, pp. 458–471, 2009.

[19] T.-L. Teng, C.-C. Liang, and Liao-Ching-Cho, “Transient Dynamic Large-Deflection Analysis of Panel Structure under Blast Loading,” *Japan Soc. Mech. Eng.*, vol. 339, no. 4, pp. 591–597, 1996.

[20] V. R. Feldgun, D. Z. Yankelevsky, and Y. S. Karinski, “A nonlinear SDOF model for blast response simulation of elastic thin rectangular plates,” *Int. J. Impact Eng.*, vol. 88, pp. 172–188, 2016.

[21] G. Chandrasekharappa and H. R. Srirangarajan, “Nonlinear response of elastic plates to pulse excitations,” *Comput. Struct.*, vol. 27, no. 3, pp. 373–378, 1987.

[22] T. Liu, W. Zhang, and J. . Wang, “Nonlinear dynamics of composite laminated circular cylindrical shell clamped along a generatrix and with membranes at both ends,” *Nonlinear Dyn.*, vol. 90, no. 2, pp. 1393–1417, 2017.

[23] A. Wang, H. Chen, and W. Zhang, “Nonlinear transient response of doubly curved shallow shells reinforced with graphene nanoplatelets subjected to blast loads considering thermal effects,” *Compos. Struct.*, vol. 225, no. May, p. 111063, 2019.

[24] J. . Reddy, *Mechanics of Laminated Composite Plates and Shells: Theory and Analysis*, 2nd ed. London: CRC Press, 2004.

[25] W. Zhang, T. Liu, A. Xi, and Y. N. Wang, “Resonant responses and chaotic dynamics of composite laminated circular cylindrical shell with membranes,” *J. Sound Vib.*, vol. 423, no. March, pp. 65–99, 2018.

[26] W. Zhang, J. Yang, and Y. Hao, “Chaotic vibrations of an orthotropic FGM rectangular plate based on third-order shear deformation theory,” *Nonlinear Dyn.*, vol. 59, pp. 619–660, 2010.

[27] N. Jacob, G. N. Nurick, and G. S. Langdon, "The effect of stand-off distance on the failure of fully clamped circular mild steel plates subjected to blast loads," *Eng. Struct.*, vol. 29, no. 10, pp. 2723–2736, 2007.
[28] C. N. Kingery and N. Bulmash, "Air blast parameters from TNT spherical air burst and hemispherical surface burst, Report ARBL-TR-02555," MD, 1984.
[29] V. Aune, G. Valsamos, F. Casadei, M. Larcher, M. Langseth, and T. Børvik, "Numerical study on the structural response of blast-loaded thin aluminium and steel plates," *Int. J. Impact Eng.*, vol. 99, pp. 131–144, 2017.
[30] D. Karagiozova, G. S. Langdon, G. N. Nurick, and S. Chung Kim Yuen, "Simulation of the response of fibre-metal laminates to localised blast loading," *Int. J. Impact Eng.*, vol. 37, no. 6, pp. 766–782, 2010.
[31] A. S. Fallah, K. Micallef, G. S. Langdon, W. C. Lee, P. T. Curtis, and L. A. Louca, "Dynamic response of Dyneema® HB26 plates to localised blast loading," *Int. J. Impact Eng.*, vol. 73, no. November, pp. 91–100, 2014.
[32] K. Micallef, A. S. Fallah, D. J. Pope, and L. A. Louca, "The dynamic performance of simply-supported rigid-plastic circular steel plates subjected to localised blast loading," *Int. J. Mech. Sci.*, vol. 65, no. 1, pp. 177–191, 2012.
[33] G. K. Schleyer, S. S. Hsu, M. D. White, and R. S. Birch, "Pulse pressure loading of clamped mild steel plates," *Int. J. Impact Eng.*, vol. 28, no. 2, pp. 223–247, 2003.
[34] V. Aune, E. Fagerholt, K. O. Hauge, M. Langseth, and T. Børvik, "Experimental study on the response of thin aluminium and steel plates subjected to airblast loading," *Int. J. Impact Eng.*, vol. 90, pp. 106–121, 2016.
[35] C. K. Youngdahl, "Correlation parameters for eliminating the effects of pulse shape on dynamic plate deformation," *Trans. ASME J. Appl. Mech.*, vol. 37, no. 2, pp. 744–752, 1970.
[36] Q. M. Li and N. Jones, "Foundation of Correlation Parameters for Eliminating Pulse Shape Effects on Dynamic Plastic Response of Structures," *J. Appl. Mech.*, vol. 72, no. 2, p. 172, 2005.
[37] Y. Yuan, P. J. Tan, K. A. Shojaei, and P. Wrobel, "Large deformation, damage evolution and failure of ductile structures to pulse-pressure loading," *Int. J. Solids Struct.*, vol. 96, pp. 320–339, 2016.
[38] A. H. Nayfeh, *Introduction to Perturbation Techniques*, vol. 20. New York: Wiley-Interscience Publication, 1993.
[39] SSAB, "Armox Blast Protection Plate," *SSAB Swedish Steel Ltd*, 2018. .
[40] T. Cwik and B. Se, "Project report : Ballistic performance of Armox 370T and Armox 440 steels," no. June, 2015.

Appendix A

A1. Stress tensor components and stiffness matrices

The significant (non-zero) components of the stress tensor (with $i \geq 1$) may be expressed as:

$$\sigma_{22}^{(i+1)} = \frac{\pi^2}{L^2} EH^2 \left[-\frac{1}{4} \bar{\Phi}_{11}^{(i+1)} \cos\left(\frac{\pi x}{2L}\right) \cos\left(\frac{\pi y}{2L}\right) - \frac{9}{4} \bar{\Phi}_{13}^{(i+1)} \cos\left(\frac{3\pi x}{2L}\right) \cos\left(\frac{\pi y}{2L}\right) - \frac{1}{4} \bar{\Phi}_{13}^{(i+1)} \cos\left(\frac{\pi x}{2L}\right) \cos\left(\frac{3\pi y}{2L}\right) - \frac{9}{4} \bar{\Phi}_{33}^{(i+1)} \cos\left(\frac{3\pi x}{2L}\right) \cos\left(\frac{3\pi y}{2L}\right) \right] \quad \textbf{(A. 45)}$$

$$\sigma_{11}^{(i+1)} = \frac{\pi^2}{L^2} EH^2 \left[-\frac{1}{4} \bar{\Phi}_{11}^{(i+1)} \cos\left(\frac{\pi x}{2L}\right) \cos\left(\frac{\pi y}{2L}\right) - \frac{9}{4} \bar{\Phi}_{13}^{(i+1)} \cos\left(\frac{\pi x}{2L}\right) \cos\left(\frac{3\pi y}{2L}\right) - \frac{1}{4} \bar{\Phi}_{13}^{(i+1)} \cos\left(\frac{3\pi x}{2L}\right) \cos\left(\frac{\pi y}{2L}\right) - \frac{9}{4} \bar{\Phi}_{33}^{(i+1)} \cos\left(\frac{3\pi x}{2L}\right) \cos\left(\frac{3\pi y}{2L}\right) \right] \quad \textbf{(A. 46)}$$

$$\sigma_{12}^{(i+1)} = \frac{\pi^2}{L^2} EH^2 \left[\frac{1}{4} \bar{\Phi}_{11}^{(i+1)} \sin\left(\frac{\pi x}{2L}\right) \sin\left(\frac{\pi y}{2L}\right) + \frac{3}{4} \bar{\Phi}_{13}^{(i+1)} \sin\left(\frac{3\pi x}{2L}\right) \sin\left(\frac{\pi y}{2L}\right) + \frac{3}{4} \bar{\Phi}_{13}^{(i+1)} \sin\left(\frac{\pi x}{2L}\right) \sin\left(\frac{3\pi y}{2L}\right) + \frac{9}{4} \bar{\Phi}_{33}^{(i+1)} \sin\left(\frac{3\pi x}{2L}\right) \sin\left(\frac{3\pi y}{2L}\right) \right] \quad \textbf{(A. 47)}$$

The coefficients of the matrix $\boldsymbol{B}_{mn}$ are given as:

$$B_{11}=\begin{bmatrix} -\frac{2}{3} & -\frac{22}{45} & -\frac{22}{45} & \frac{2}{5} \\ -\frac{22}{45} & -\frac{114}{35} & -\frac{166}{225} & -\frac{162}{175} \\ -\frac{22}{45} & -\frac{166}{225} & -\frac{114}{35} & -\frac{162}{175} \\ \frac{2}{5} & -\frac{162}{175} & -\frac{162}{175} & -\frac{162}{35} \end{bmatrix} \tag{A-48}$$

$$B_{13}=\begin{bmatrix} -\frac{22}{45} & -\frac{166}{225} & -\frac{114}{35} & -\frac{162}{175} \\ -\frac{166}{225} & -\frac{186}{35} & -\frac{186}{35} & -\frac{26406}{1225} \\ -\frac{114}{35} & -\frac{166}{225} & 2 & -\frac{22}{15} \\ -\frac{162}{175} & -\frac{26406}{1225} & -\frac{22}{15} & \frac{342}{35} \end{bmatrix} \tag{A-49}$$

$$B_{33}=\begin{bmatrix} \frac{2}{5} & -\frac{162}{175} & -\frac{162}{175} & -\frac{162}{35} \\ -\frac{162}{175} & \frac{22}{15} & -\frac{26406}{1225} & \frac{342}{35} \\ -\frac{162}{175} & -\frac{26406}{1225} & \frac{22}{15} & \frac{342}{35} \\ -\frac{162}{35} & \frac{342}{35} & \frac{342}{35} & -6 \end{bmatrix} \tag{A-50}$$

The components of Airy Stress function are expressed as:

$$\bar{\phi}_{11}^{(\mathrm{i}+1)}=-\frac{4}{\pi^2}\left\{\frac{1}{3}\bar{w}_{11}^{(i)^2}+\frac{44}{45}\bar{w}_{11}^{(i)}\bar{w}_{13}^{(i)}+-\frac{2}{5}\bar{w}_{11}^{(i)}\bar{w}_{33}^{(i)}+\frac{6292}{1575}\bar{w}_{13}^{(i)^2}+\frac{324}{175}\bar{w}_{13}^{(i)}\bar{w}_{33}^{(i)}+\frac{81}{35}\bar{w}_{33}^{(i)^2}\right\} \tag{A. 51}$$

$$\begin{aligned}\bar{\phi}_{13}^{(i+1)}=-\frac{4}{275625\pi^2}\Big\{&2695\bar{w}_{11}^{(i)^2}+44044\bar{w}_{11}^{(i)}\bar{w}_{13}^{(i)}+10206\bar{w}_{11}^{(i)}\bar{w}_{33}^{(i)}+76860\bar{w}_{13}^{(i)^2}\\&+221484\bar{w}_{13}^{(i)}\bar{w}_{33}^{(i)}-53865\bar{w}_{33}^{(i)^2}\Big\}\end{aligned} \tag{A. 52}$$

$$\begin{aligned}\bar{\phi}_{33}^{(i+1)}=-\frac{4}{297675\pi^2}\Big\{&735\bar{w}_{11}^{(i)^2}-6804\bar{w}_{11}^{(i)}\bar{w}_{13}^{(i)}-170106\bar{w}_{11}^{(i)}\bar{w}_{33}^{(i)}-73828\bar{w}_{13}^{(i)^2}\\&+71820\bar{w}_{13}^{(1)}\bar{w}_{33}^{(1)}-11025\bar{w}_{33}^{(1)^2}\Big\}\end{aligned} \tag{A. 53}$$

and $\bar{\phi}_{ij}^{(i)} = \bar{\phi}_{ji}^{(i)}$ as the Airy Stress function exhibits symmetry.

A2. Second phase of motion parameters

Regarding the first mode of the displacement field at second phase of motion we have:

$$\begin{aligned} f(\tau_{11}) \cong -\frac{E c_{11}^3}{L^2 \omega_{11}^2 \rho} \Big(& 0.0395\big(cos(3\tau_{11}) - cos(3\tau_{11} - 3\bar{t_d})\big) \\ &+ 0.098\big(cos(3\tau_{11} - 2\bar{t_d}) - cos(3\tau_{11} - \bar{t_d})\big) \\ &+ 0.0134\big(cos(3\tau_{11} - 4\bar{t_d}) - cos(3\tau_{11} + \bar{t_d})\big) \\ &+ 0.598\big(cos(\tau_{11} - \bar{t_d}) - cos(\tau_{11})\big) \\ &+ 0.196\big(cos(\tau_{11} + \bar{t_d}) - cos(\tau_{11} - 2\bar{t_d})\big)\Big) \end{aligned} \quad \textbf{(A-54)}$$

Where the integration constants

$$\begin{aligned} C_4 = \frac{c_{11}^3 E}{L^2 \rho \omega_{11}^2} \big(-1.6cos(\bar{t_d}) + 2.0753 - 0.269cos(2\bar{t_d}) - 0.192cos(3\bar{t_d})\big) \\ + \frac{c_{11}\bar{\omega}_{11}}{2\omega_{11}}\big(1 - cos(\bar{t_d})\big) \end{aligned} \quad \textbf{(A. 55)}$$

$$\begin{aligned} C_5 \cong \frac{E c_{11}^3}{\rho L^2 \omega_{11}^2} \big(-0.27sin(2\bar{t_d}) + -0.1946sin(3\bar{t_d}) - 0.0015sin(7\bar{t_d}) - 3.2940sin(\bar{t_d})\big) \\ - \frac{c_{11}\bar{\omega}_{11}}{2\omega_{11}} sin(\bar{t_d}) \end{aligned} \quad \textbf{(A. 56)}$$

Similarly, for the higher modes:

$$\begin{aligned} f(\tau_{13}) \cong \frac{c_{13}^3 E}{\omega_{13}^2 \rho\, L^2} \Big(& -5616cos(0.6\tau_{13} + 0.2\bar{t_d}) - 16460cos(0.6\tau_{13} - 0.2\bar{t_d}) \\ & - 3744cos(1.4\tau_{13} - 1.2\bar{t_d}) - 34080cos\big(0.2(\tau_{13} - \bar{t_d})\big) \\ & - 2808cos(0.6\tau_{13} - \bar{t_d}) + 3744cos(1.4\tau_{13} - 0.2\bar{t_d}) \\ & + +5616cos(0.6\tau_{13} - .8\bar{t_d}) + 8294cos(0.6\tau_{13}) \\ & - 10970\cos\big(0.2(\tau_{13} + \bar{t_d})\big) + 2808cos(0.6\tau_{13} + 0.4\bar{t_d}) \\ & - 8294cos(0.6\tau_{13} - 0.6\bar{t_d}) + 16460cos(0.6\tau_{13} - 0.4\bar{t_d}) \\ & + 10970cos(.2\tau_{13} - .4\bar{t_d}) + 34080cos(0.2\tau_{13})\Big) \\ & + \frac{\bar{\omega}_{13}}{2\omega_{13}} c_{13}\big(cos(\tau_{13} - tdbar) - cos(\tau_{13})\big) \end{aligned} \quad \textbf{(A-57)}$$

$$\begin{aligned} C_6 \cong \frac{c_{13}\bar{\omega}_{13}}{2\omega_{13}}\big(1 - cos(\bar{t_d})\big) - \frac{E c_{13}^3}{L^2 \omega_{13}^2\, \rho}(& 1733cos(2\bar{t_d}) + 566.3cos(2.2\bar{t_d}) + 2485cos(0.6\bar{t_d}) \\ & + 1465cos(1.2\bar{t_d}) - 1493cos(1.4\bar{t_d}) - 1797cos(0.2\bar{t_d}) \\ & + -6609cos(.8\bar{t_d}) + 43.52cos(3.2\bar{t_d}) + 426.7cos(1.8\bar{t_d}) + 4217cos(\bar{t_d}) \\ & - 1012) \end{aligned} \quad \textbf{(A. 58)}$$

$$C_7 = -\frac{c_{13}\overline{\omega}_{13}}{2\omega_{13}} sin(\overline{t_d}) - \frac{Ec_{13}^3}{L^2\omega_{13}^2\rho}(1733sin(2\overline{t_d}) + 566.3sin(2.2\overline{t_d}) + 2485sin(.6\overline{t_d}) + 1697sin(1.2\overline{t_d}) - 1493sin(1.4\overline{t_d}) + 49.72sin(2.8\overline{t_d}) - 75.78sin(3\overline{t_d}) + 27199sin(0.2\overline{t_d}) - 6261sin(0.8\overline{t_d}) + 43.52sin(3.2\overline{t_d}) + 426.7sin(1.8\overline{t_d}) + 3805sin(\overline{t_d}) \tag{A. 59}$$

Full expression of $\overline{w}_{33}^{(1)}$ is given as:

$$\overline{w}_{33}^{(1)} = -\frac{c_{11}^3 E}{L^2\omega_{33}^2\rho}\Bigg(0.106cos(\tau_{33}) - 0.882 + 3.79\times10^{-4}cos(2\tau_{33}) + 0.105cos\left(\frac{10}{3}\tau_{33}\right) + 1.48cos\left(\frac{10}{9}\tau_{33}\right) + 3.28\times10^{-4}cos(1.44\tau_{33}) + 8.05\times10^{-4}cos\left(\frac{5}{3}\tau_{33}\right) - 2.24\times10^{-4}cos\left(\frac{17}{9}\tau_{33}\right) + 0.0799cos\left(\frac{11}{9}\tau_{33}\right) + 1.87\times10^{-4}cos\left(\frac{19}{9}\tau_{33}\right) - 0.186cos\left(\frac{7}{9}\tau_{33}\right) + 0.449cos\left(\frac{2}{3}\tau_{33}\right) - 0.741cos\left(\frac{2}{9}\tau_{33}\right) - 0.619cos\left(\frac{5}{9}\tau_{33}\right) - 3.81\times10^{-3}cos\left(\frac{14}{9}\tau_{33}\right) - 0.583cos\left(\frac{10}{9}\tau_{33}\right) + 0.477cos\left(\frac{8}{9}\tau_{33}\right) + 0.318cos\left(\frac{4}{9}\tau_{33}\right)\Bigg) \tag{A-60}$$

A3. Dynamic pulse pressure loading

The integration constants of the displacement field considering the influence of pulse shape are:

$$G_1 = \Big\{\Big(\omega_{mn}^2 t_d^2\big((X-1)Y - X\big) + Y^2\big((X-1)Y + X\big)\Big)cos(\omega_{mn}t_d) - \omega_{mn}t_d sin(\omega_{mn}t_d)\Big(\omega_{mn}^2 t_d^2(X-1) + Y\big((X-1)Y + 2X\big)\Big)\Big\}e^{-Y} + t_d^2\omega_{mn}^2(X+Y) - Y^2(X-Y) \tag{A. 61}$$

$$E_1 = -\Big(\Big\{\Big(t_d^2\big((X-1)Y - X\big)\omega_{mn}^2 + Y^2\big((X-1)Y + X\big)\Big)sin(\omega_{mn}t_d) + \Big(t_d^2\omega_{mn}^2(X-1) + Y\big((X-1)Y + 2X\big)\Big)cos(\omega_{mn}t_d)\omega_{mn}t_d\Big\}e^{-Y} + \omega_{mn}^3 t_d^3 + Y^2 - 2XY\omega_{mn}t_d\Big) \tag{A. 62}$$

For a linear pulse shape, $Y = 0$, Eq. (44) is reduced to:

$$w_{mn}^{(1)} = -\frac{c_{mn}}{\omega_{mn}t_d}\big(G_2 sin(\omega_{mn}t) + E_2 cos(\omega_{mn}t)\big) \tag{A. 63}$$

$$G_2 = \big(X(cos(\omega_{mn}t_d) - 1) + \omega_{mn}t_d(X-1)sin(\omega_{mn}t_d)\big) \tag{A. 64}$$

$$E_2 = (\omega_{mn}t_d(X-1)cos(\omega_{mn}t_d) - Xsin(\omega_{mn}t_d) + \omega_{mn}t_d) \tag{A. 65}$$

Carrying out some algebraic manipulation, the deformation of the plate for a linear pulse shape is expressed as

$$w_{mn}^{(1)} = -\boldsymbol{W_2} sin(\omega_{mn} t + \beta_2) \tag{A. 66}$$

$$\boldsymbol{W_2} = \frac{c_{mn}}{\omega_{mn} t_d} \sqrt{E_2^2 + G_2^2}\,, \beta_2 = \tan^{-1} E_2/G_2 \tag{A. 67}$$

In the same fashion, Eq. (44) may be recast in the form of $\boldsymbol{W_3} sin(\omega_{mn} t + \beta_3)$ where the maximum deformation of exponentially attenuating pulse is expressed as

$$\boldsymbol{W_3} = \frac{c_{mn} \omega_{mn} t_d}{(\omega_{mn}^2 t_d^2 + Y^2)^2} \sqrt{E_3^2 + G_3^2}\,, \beta_3 = \tan^{-1} E_2/G_2 \tag{A. 68}$$

$$G_3 = \big((-Y\omega_{mn}^2 t_d^2 - Y^3) cos(\omega_{mn} t_d) - \omega_{mn} t_d sin(\omega_{mn} t_d)(-\omega_{mn}^2 t_d^2 - Y^2)\big) e^{-Y} + Y\omega_{mn}^2 t_d^2 + Y^3 \tag{A. 69}$$

$$E_3 = (\omega_{mn}^2 t_d^2 + Y^2)((\omega_{mn} t_d cos(\omega_{mn} t_d) + sin(\omega_{mn} t_d) Y) e^{-Y} - \omega_{mn} t_d) \tag{A. 70}$$